Editors' Suggestion

Microwave-free imaging magnetometry with nitrogen-vacancy centers in nanodiamonds at near-zero field

Saravanan Sengottuvel,[1,2,*,‡] Omkar Dhungel,[3,4,‡] Mariusz Mrózek,[2] Arne Wickenbrock,[3,4,5] Dmitry Budker,[3,4,5,6] Wojciech Gawlik,[2] and Adam M. Wojciechowski[2,†]

[1] *Doctoral School of Exact and Natural Sciences, Jagiellonian University, Łojasiewicza 11, 30-348 Kraków, Poland*

[2] *Institute of Physics, Jagiellonian University, Łojasiewicza 11, 30-348 Kraków, Poland*

[3] *Helmholtz-Institut Mainz, 55099 Mainz, Germany*

[4] *Johannes Gutenberg-Universität Mainz, 55128 Mainz, Germany*

[5] *GSI Helmholtzzentrum für Schwerionenforschung GmbH, 64291 Darmstadt, Germany*

[6] *Department of Physics, University of California, Berkeley, California 94720-7300, USA*

(Received 5 September 2024; revised 14 January 2025; accepted 31 January 2025; published 3 March 2025)

Magnetometry using nitrogen-vacancy (N-V) color centers in diamond predominantly relies on microwave spectroscopy. However, microwaves may hinder certain studies involving biological systems or thin conductive samples. This work demonstrates a wide-field, microwave-free imaging magnetometer utilizing N-V centers in nanodiamonds by exploiting the cross-relaxation feature near zero magnetic fields under ambient conditions without applying microwaves. For this purpose, we measure the center shift, contrast, and linewidth of zero-field cross relaxation in 140-nm nanodiamonds dropcast on a current-carrying conductive pattern while scanning a background magnetic field, achieving a sensitivity of 4.5 $\mu\mathrm{T}/\sqrt{\mathrm{Hz}}$. Our work allows for applying the N-V zero-field feature in nanodiamonds for magnetic-field sensing in the zero- and low-field regimes and highlights the potential for microwave-free all-optical wide-field magnetometry based on nanodiamonds.

DOI: 10.1103/PhysRevApplied.23.034001

I. INTRODUCTION

The application of negatively charged nitrogen-vacancy (N-V^-) color centers in diamond [1] has become the focal point for sensing physical parameters, such as temperature, pressure, magnetic and electric fields at the nanoscale, even under challenging environmental conditions [2–6]. N-V centers have shown remarkable sensitivities in recent years, reaching 0.5 $\mathrm{pT}/\sqrt{\mathrm{Hz}}$ for ensembles at room temperature [7]. The use of N-V centers for magnetometry allows the exploration of magnetic fields generated by various samples, including biological systems, magnetic materials, and current-carrying wires [8–11]. Many magnetic-measurement applications using N-V centers rely on optically detected magnetic resonance (ODMR) with microwave fields and the application of external magnetic fields to remove the degeneracy of the spin sublevels. However, these techniques can be challenging for systems where external magnetic fields and high-power microwaves interfere with the sample or where microwaves are invasive, such as in high-transition-temperature (T_c) superconductors, zero- to ultra-low-field nuclear magnetic resonance (ZULF NMR), two-dimensional magnetic materials, and biological samples [12,13].

To address these problems, microwave-free protocols have been developed, exploiting energy-level crossings involving N-V centers at zero and specific nonzero magnetic fields, such as the cross-relaxation features in the fluorescence spectrum of N-V centers at near zero B fields [14–17], the level anticrossing within the triplet ground state at 102.4 mT and the N-V–P1 crossing at 51.2 mT [18–22]. In addition to the nonzero field crossings, the electronic sublevels of the N-V center cross also at a zero B field [23–25]. Each level crossing reflects the related degeneracy in the system that makes it prone to perturbations that may mix the quantum states and alter their populations, which is known as cross relaxation [26]. We

*Contact author: saravanan.sengottuvel@doctoral.uj.edu.pl

†Contact author: a.wojciechowski@uj.edu.pl

‡These authors contributed equally to this work.

assume that the measured magnetic field is the sum of an unknown constant field and a scanned field. In this scenario, the zero-field cross-relaxation feature position depends on the constant field and can be used to infer the unknown magnetic field.

This work focuses on the implementation of a practical N-V magnetometer utilizing the zero-field cross-relaxation feature. Specifically, we present a microwave-free magnetometer that leverages the cross-relaxation feature at zero field to map magnetic fields above a current-carrying cross pattern coated with N-V nanodiamonds. The use of nanodiamonds facilitates imaging on arbitrarily shaped surfaces. Our findings highlight the potential of zero-field magnetometry for real-world applications.

II. ZERO-FIELD MICROWAVE-FREE N-V MAGNETOMETRY

Numerous studies have been carried out recently to understand N-V cross-relaxation characteristics near zero field. Although not all aspects of longitudinal relaxation (T_1) in dense ensembles are fully understood [27], one hypothesis involves "fluctuator" defects, which depolarize nearby N-Vs, leading to depolarization of the entire sample via dipolar interactions [28]. In addition, there is also a relaxation mechanism associated with local electric fields and the interaction between N-V centers oriented similarly and differently, which is particularly relevant in high-density samples [29]. The zero-field cross-relaxation feature and additional features observed in the presence of a bias field have been systematically examined as a function of N-V density, magnetic-field orientation, and temperature [30]. Similar characteristics have also been identified in nanodiamonds, and their behavior has been investigated in terms of nanodiamond size and light intensity. Specifically, the authors of Ref. [31] investigated how variations in N-V density, orientation, nanodiamond size, and light intensity influence observed characteristics, providing a significant understanding of the interplay of these factors in the studied phenomena.

Magnetometry with nanodiamonds offers advantages over other N-V-diamond sensors. Conventional N-V magnetometry often involves the use of bulk diamond or thin N-V layers or employs scanning diamond tips to reduce the standoff distance to the sample, typically down to several nanometers for AFM-type sensors, to achieve high sensitivity and spatial resolution when mapping magnetic fields [32]. However, these methods have limitations as they require a smooth sample surface and proximity of the sample to the measurement diamond. In contrast, the small size of the nanodiamonds allows them to be bonded to irregular material surfaces, including fiber tips and living cells [33,34].

In this study, we used the "salt-and-pepper" approach [31] using randomly oriented nanodiamonds containing N-V centers to create a cost-effective and straightforward wide-field magnetometer without microwaves for near-zero-field measurements. The sensitivity of these N-V–ND magnetometers can reach below the $\mathrm{nT}/\sqrt{\mathrm{Hz}}$ level [35], with typical per-pixel sensitivities in the case of imaging devices of a few $\mu\mathrm{T}/\sqrt{\mathrm{Hz}}$ [36]. The biocompatibility of NDs allows their use in biomedical applications, such as magnetic resonance imaging (MRI) of the brain and other organs [37]. Furthermore, the small size of NDs enables nanoscale spatial resolution, making them ideal for imaging the magnetic fields of biological structures at the cellular and subcellular levels [38]. The utilization of nanodiamonds presents a balanced compromise between sensitivity, resolution, and manufacturing costs. Another significant advantage of our method is the implementation of wide-field magnetic imaging without microwaves, eliminating all the effects of microwaves, enabling real-time parallel mapping of the magnetic field across a large field of view, and reducing measurement time.

III. EXPERIMENTAL SETUP

The diamonds used in this work are commercially available 140-nm carboxylated fluorescent nanodiamonds by Adamas Nanotechnologies. A suspension of these diamonds in deionized (DI) water is deposited onto a transparent polyethylene terephthalate (PET) substrate, which has a thickness of 0.11 mm, using the drop-casting technique. The sample is then allowed to air dry for 15–30 min. On the reverse side of the PET substrate, a copper cross pattern, with wires 65 μm wide, is printed and subsequently fixed to a printed circuit board (PCB). This cross pattern comprises four individual arms [labeled 1 to 4 in Fig. 1(b)] that intersect at the center. The pattern is connected to a power source, allowing the current to be driven through any specific path (e.g., 1–2, 1–4) across the pattern. The salt-and-pepper technique is a straightforward method involving the direct drop casting of nanodiamonds held in water suspension on a planar surface, later dried in air, thus forming a relatively stable thin film held by van der Waals forces and gravity. However, the stability of nanodiamonds can be affected by thermal effects arising from external sources, such as lasers and microwaves. In our study, the use of microwaves was eliminated, leaving laser excitation as the sole potential heating source. Positional instability or drift of nanodiamonds may occur due to thermal effects when employing high laser power or conducting prolonged measurements [36].

For N-V magnetometry described here, a home-built wide-field fluorescence microscope was used, as shown in Fig. 1(a). The nanodiamond sample was illuminated with 60–70 mW of 532-nm green light from an LED (Thorlabs M530L4). The light beam was collimated with an aspheric condenser lens (focal length 50 mm) and guided

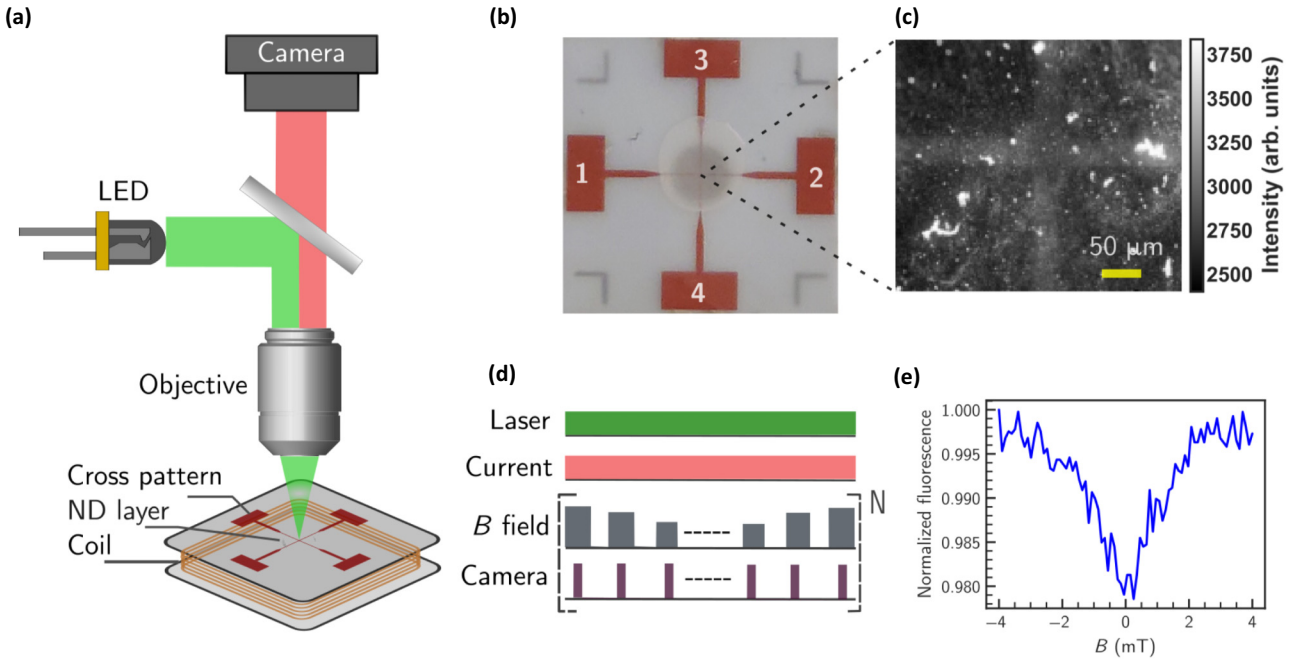

FIG. 1. (a) Schematic of the wide-field magnetic imaging setup, (b) the conductive cross pattern embedded in a transparent substrate attached to a PCB with NDs deposited at the interjunction, (c) a single-shot microscopic fluorescence image of N-V centers with the cross pattern in the background, (d) sequence of the measurement and imaging protocol, (e) near-zero-field fluorescence spectrum of the nanodiamonds.

with a dichroic mirror to the back focal plane of a 40× Olympus microscope objective with a numerical aperture of 0.65. The pump beam focused with the objective illuminates the nanodiamonds. The red fluorescence emitted from the N-V centers is collected using the same microscope objective and imaged with a Basler camera equipped with a 12-bit Sony CMOS sensor. In our imaging system, the field of view (FOV) of the camera is 2448 × 2048 pixels, which correspond to an area of 384 μm × 321 μm on the nanodiamond layer with 0.15 μm × 0.15 μm per pixel. Given that the mean size of the nanodiamonds is approximately 140 nm, taking into account additional blur caused by optical diffraction, we estimate that each pixel typically contains one or two nanodiamonds, with possible occasional overlapping of more nanodiamonds. A square dc current-carrying coil (with $N = 20$ turns and length $R_{\text{coil}} = 50$ mm) creates a bias field perpendicular to the N-V imaging plane.

The N-V magnetometer was calibrated using a test magnetic field. The magnetic field of the current-carrying coil was cross-verified by measuring the Zeeman splitting along the quantization axis (⟨111⟩ crystallographic directions) of one of the N-V orientations in a (100)-cut thin monocrystal diamond sample. The estimated magnetic field value from the N-V ODMR splitting is consistent with the applied test magnetic field calculated based on the coil current and its geometry.

IV. RESULTS AND DISCUSSIONS

A. Imaging of static magnetic fields using nanodiamonds

In this section, we describe the methodology to image and map the magnetic field generated with a cross pattern for various current intensities and paths. As illustrated in Fig. 1(d), both the laser and the dc remain constant throughout the measurement. The background magnetic field applied perpendicular to the plane of the ND layer is systematically scanned in steps from −4.0 to +4.0 mT with the corresponding images captured sequentially.

Before the current measurements, we experimentally verified the presence of the zero-field feature in the NDs in the absence of current in the cross. Next, the nonzero current in the cross pattern was applied in two specific directions: (i) path 3 to 4 and (ii) path 1 to 4. We took the measurement several times and averaged the resulting images to improve the signal-to-noise ratio (SNR). In our measurements, a single scan typically lasts about 2 to 3 min, substantially faster than confocal or atomic force microscopy (AFM) scanning methods. Although two or three scans were sufficient to detect the zero-field cross-relaxation spectrum with a good SNR, to generate high-quality magnetic-field maps and reduce the background noise, we averaged over multiple scans, as the SNR improves as $\sqrt{N}$, where N is the number of scans.

The zero-field parameter maps presented in this work were generated by averaging 10 scans, resulting in a total acquisition time of approximately 20 min. Further reduction in measurement time is feasible, analogous to the two-point detection technique [39] commonly employed in optically detected magnetic resonance (ODMR) temperature measurements. For a given current path in the cross structure, we scan the magnetic field and record the fluorescence image of the ND layer. From the acquired image data, we then extract the zero-field cross-relaxation spectrum for each pixel of the camera. To reduce the relative noise of each pixel and the amount of data to be processed, we binned 16×16 pixels, thus reducing the total number of pixels by a factor of 256. The extracted spectrum is then fitted with a Gaussian function (1) to estimate the shift of the central dip (ΔB), full width at half maximum (w), and the contrast (C) of the zero-field cross-relaxation feature.

$$f(x; \Delta B, C, w) = y_0 + C \cdot \frac{1}{w\sqrt{2\pi}} e^{-((x-\Delta B)^2/2w^2)}. \quad (1)$$

Here, the parameters y_0, C, ΔB, and w are, respectively, the offset, amplitude, center, and width of the distribution. An additional magnetic field generated by the cross pattern in both parallel and perpendicular directions to the scanned field affects the parameters ΔB, C, and w of the zero-field feature. The shift ΔB is equal to the strength of the B field generated above the cross pattern. Quantifying these parameters spatially provides information about the field generated by the cross pattern. Using these estimated values, we create ΔB, C, and w maps for the entire FOV of the camera under two different current paths at 0, 0.3, and 0.5 A, as shown in Fig. 2.

As expected, when there is no current (0 A) flowing through the conductive cross pattern, we see no visible trace of the pattern on the map ΔB, which is expected. However, when the current is nonzero (0.3 and 0.5 A), the arms of the cross pattern (the central white region), through which the current flows, become visible. Notably, ΔB above the cross pattern is zero, regardless of the current path, from 3 to 4 or 1 to 4. This is because the magnetic field generated by the conductive cross pattern is perpendicular to the scanned field and does not affect it. The strength of the magnetic field decreases with distance from the center of the wire, which is observable in the shift maps. The color scheme on the ΔB map indicates that the magnetic field generated by the wire is either parallel (red) or antiparallel (blue) to the scanned field. The thickness of the wire estimated from the map agrees with the actual dimensions. The marked squares on the left and right sides of the pattern indicate the selected pixel locations and their corresponding spectra are shown in Fig. 2 to the right of the maps. The spectra extracted from the binned image data visualize the center shift when a current is applied; ΔB is positive with a higher current and negative when the current is reversed.

The C, and w maps provide complementary information to the shift maps. At 0 A, with no current flowing through the conductive cross pattern, we observed a maximum contrast of the zero-field feature of around 1% and a minimum width of 2 mT for nanodiamonds throughout the FOV. As the current increases, the overall contrast of the zero-field feature reduces, and its width increases, as evident from the colormaps at 0.3 and 0.5 A. This occurs because the magnetic field from the cross pattern tunes the electron spin splitting of the N-V centers into resonance with many surrounding N-V centers that are randomly oriented. This results in less-enhanced cross relaxation through magnetic dipole interactions with neighboring N-V centers, leading to higher fluorescence emission. At 0 A, unlike the ΔB maps, we observe a trace of the conductive cross pattern on the contrast and width maps, although it is less pronounced in the latter. This trace is due to the reflective nature of the copper structure.

Additionally, Fig. 2 shows a nonuniformity of contrast and width around the cross pattern, where the current is maximum at the center and decreases toward the edges of the maps. This suggests the presence of a nonuniform N-V layer and nanodiamond clusters, possibly resulting from the aggregation of nanodiamonds during deposition on the PET surface. Also, "oasislike" structures are seen in the width map, which may be due to the failure of the fitting function to model the data accurately.

Figure 3 shows the map of the zero-field parameters and cross-section plots of the parameters for an applied current of 0.5 A. The plot observed for ΔB, obtained by selecting one row of the image data perpendicular to the current carrying wire, shows that the maximum (minimum) shift occurs when the applied test field is parallel (antiparallel) to the scanning background field and decreases with distance from the center. The shift is zero in the center of the wire, while C is minimum and w is maximum there.

Our measurements show that the changes in ΔB, C, and w are proportional to the current applied to the wire in the relevant distance ranges. Figure 4 shows that the fit parameters vary depending on the current value in the cross pattern. The parameters were measured for a pixel near the conductive cross pattern. It is evident from the experimental results (Fig. 2) that ΔB is a direct measure of the magnetic field strength. As the current increases, ΔB also increases. On the other hand, the C and w provide complementary information. These parameters typically depend on the concentration of N-V and the transverse magnetic fields. In particular, at low currents (<0.1 A), the change in C and w are subtle. Here, we observe a linear dependence of the parameters ΔB and w on the current, whereas the C appears to scale nonlinearly. In addition, a transverse magnetic field would affect the linewidth of the zero-field spectrum. A transverse field causes nonlinear shifts and

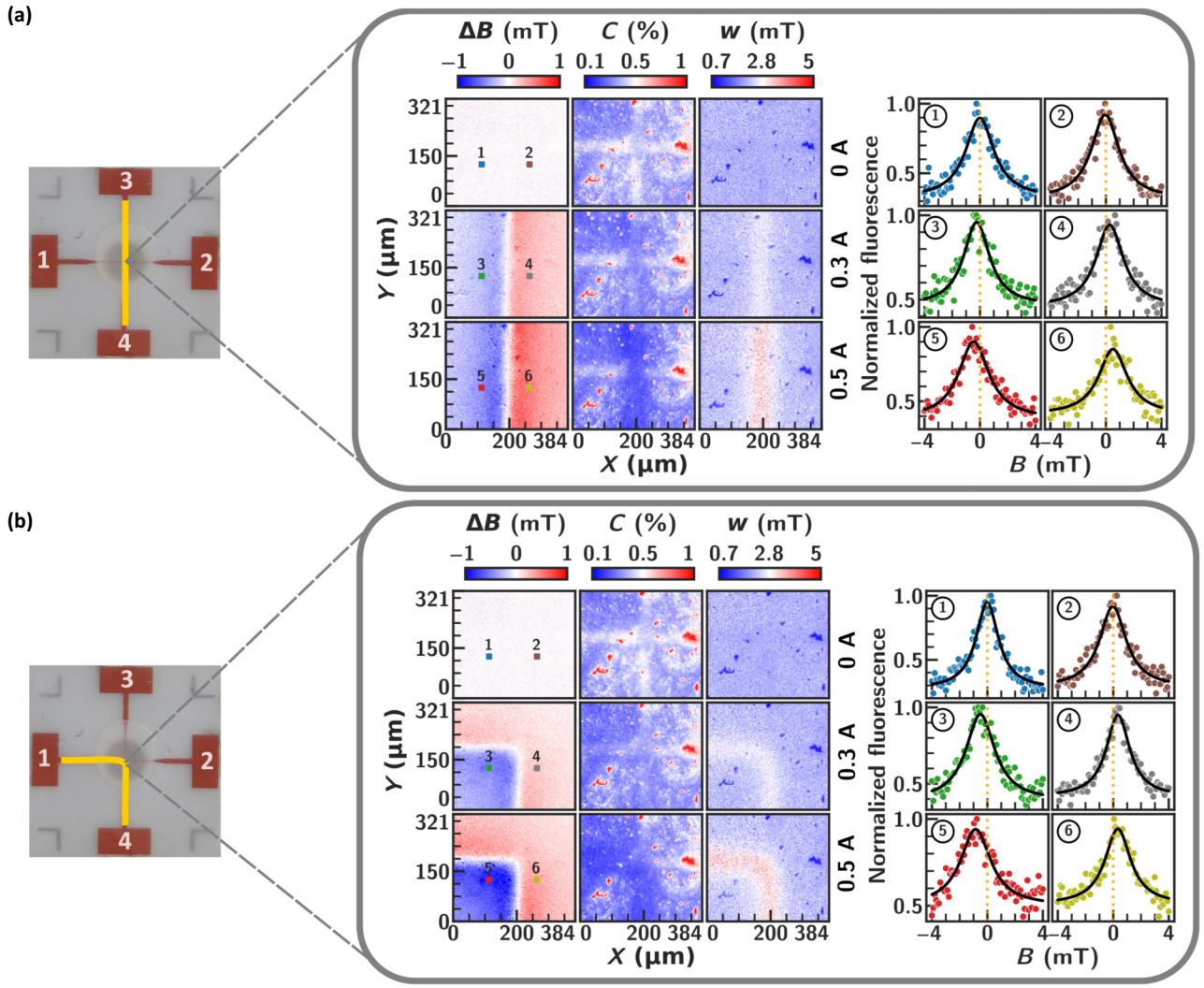

FIG. 2. Maps of the shift ΔB, contrast C, and width w of zero-field spectra for two current paths in the cross pattern with varying current intensities of 0, 0.3, and 0.5 A. (a) The current path is from point 3 to 4. (b) The current path is from point 1 to 4. The plots to the right of the maps are the single-pixel zero-field spectra extracted from the binned image data. The pixel locations are colored in the width maps.

mixing of the N-V spin states, which broadens the resonance. By measuring the linewidth, one can infer the presence of any transverse (B_x and/or B_y) component of the magnetic field.

B. Numerical simulations

To cross validate our microwave-free magnetometry scheme, we performed a numerical simulation. Numerical integration was performed using the open-source Python package Magpylib [40]. The simulated B-field distributions for two different current paths are shown in Fig. 5. The current-induced fields are directly derived from the Biot-Savart law. The magnetic-field distribution map in the x-y plane was calculated at 0.11 mm along the Z axis from the cross structure to account for the thickness of the substrate. As can be seen, there is a good agreement between the simulation and our measurements.

C. Single-pixel magnetic-field sensitivity

The photon shot-noise-limited magnetic-field sensitivity of an N-V ensemble magnetometer (similarly to that of a continuous-wave ODMR imaging protocol) is given by [41,42]

$$\delta B = P_F \frac{h}{g\mu_B} \frac{\Gamma}{C \cdot \sqrt{I_0}}. \tag{2}$$

Here Γ is the FWHM resonance linewidth, C is the contrast, $P_F \approx 0.70$ for a Gaussian-shaped resonance peak, I_0 is the photon detection rate. Here, the detected photon rate

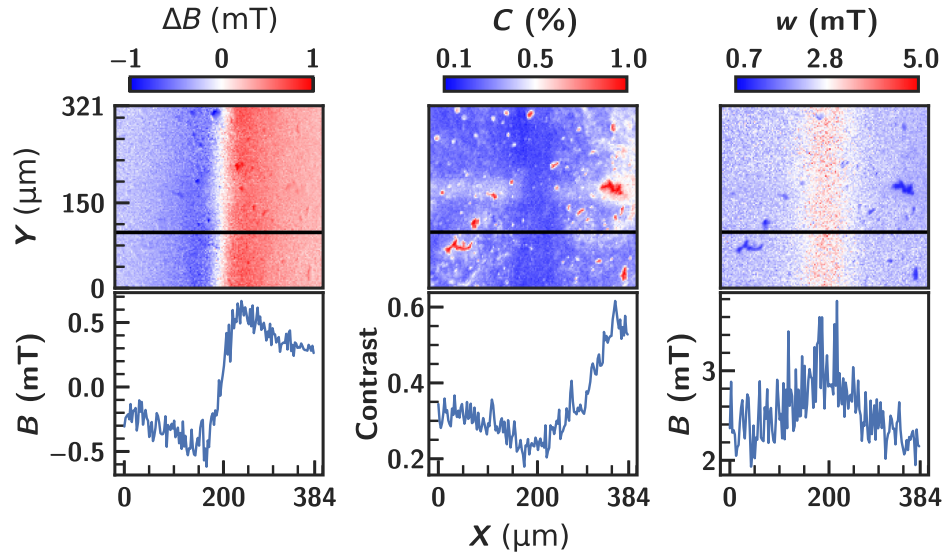

FIG. 3. The first row shows maps of the center shift (ΔB), contrast (C), and width (w) of the zero-field feature at 0.5 A. The second row shows the z component of the magnetic field, contrast, and width as a function of distance from the cross for a specific row of pixels marked by a black horizontal line in the upper row images.

is defined in terms of the number of photon counts per pixel per second, taking into account the sensor quantum efficiency. Equation (2) can be applied similarly to estimate the N-V magnetic-field sensitivity using the zero-field feature since the feature width and the contrast primarily depend on the number of N-V centers in the nanodiamonds. Due to the random orientation of the N-V centers in NDs and the variation in the number of nanodiamonds per pixel, we estimate that the mean per-pixel sensitivity of our ND magnetometer is approximately 4.5 $\mu T/\sqrt{Hz}$ (approximately equal to 9×10^6 counts per second for an effective sample area of $0.02\,\mu m^2$). The estimated sensitivity of our current imaging instrument corresponds to the field sensed by a 140-nm nanodiamond sitting at a distance of 110 μm above the cross pattern. In our experiment, this sensitivity was sufficient to detect B fields (<1 mT) when applying a few mA of current.

The sensitivity can be further improved by reducing the stand-off distance between the N-V layer and the current source, which would allow the detection of smaller magnetic fields and increase the precision of source localization. In principle, the nanodiamonds could be deposited on the same side of the substrate where the cross pattern is attached, thereby reducing the distance between the nanodiamonds and the electrode structure. Additionally, sensitivity can be improved using higher-NA optics (increases fluorescence collection efficiency), higher laser power, faster camera with lower read-out noise, and lock-in camera detection.

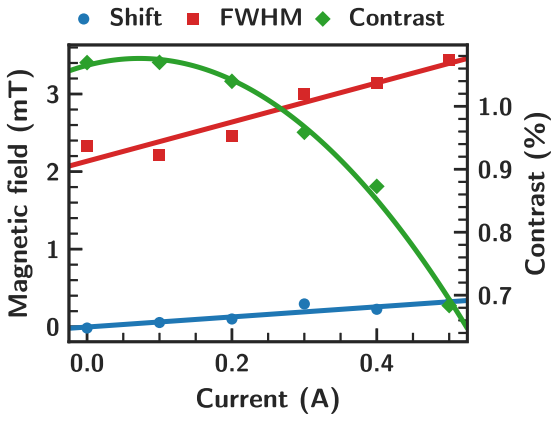

FIG. 4. Change in the parameters of zero-field feature fit measured close to the cross pattern as a function of the applied current (ΔB, w correspond to the left scale, and C to the right scale).

V. CONCLUSIONS

In this study, we have shown that the zero-field cross-relaxation feature can be effectively used for imaging and mapping the magnetic-field distribution. As a proof-of-concept potential application, we successfully visualized the magnetic field produced by a current-carrying wire pattern using N-V ensembles in nanodiamonds. In this work, we characterized three key parameters of the zero-field feature: center, width, and contrast for different current intensities. Additionally, we validated our experimentally observed magnetic-field distribution of the cross pattern through numerical simulations. In particular, the feature exhibits a broader linewidth approximately equal to 2.0 mT and a lower contrast of approximately 1–2% in NDs compared to some single-crystal diamond samples with high N-V concentrations (approximately equal

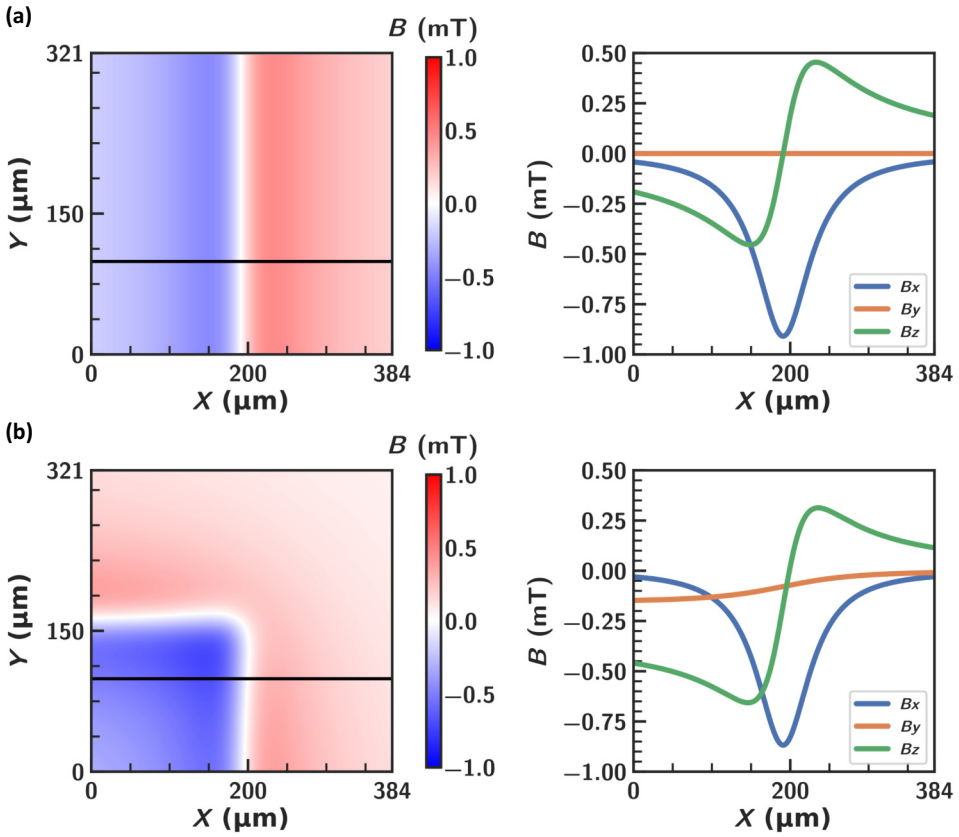

FIG. 5. Numerical simulation of the B-field distribution at a distance of 0.11 mm from the surface of the cross pattern with an applied current of 0.5 A in two specific directions (a) path 3 to 4 and (b) path 1 to 4. The plots adjacent to the maps show the components of the B field along the black line.

to 0.2 mT) linewidth and approximately equal to 4% contrast [30].

The fact that the zero-field technique does not require a microwave or precise orientation of a known magnetic field makes it unique among other N-V magnetometers. The zero-field technique may find applications in biosensing since the lack of microwave field is a significant advantage when studying cells, and nanodiamonds are already readily used as trackers for fluorescence microscopy. It could also be used for real-time magnetometry in living cells with diamonds without having to constantly calibrate the diamond axes using ODMR and other microwave-based techniques. Thanks to the application of nanodiamond coatings, the method can be very useful for imaging of arbitrary-shaped surfaces.

The B field is scanned in steps at a constant rate and when experiments involve thin conductive materials (e.g., graphene, transition-metal dichalcogenides), spikes of eddy currents might be expected in the sample, albeit they should decay quickly (within milliseconds). Consider a conductor with a characteristic area A, thickness t, and resistivity ρ. The induced voltage is $A(dB/dt)$, and the current is the induced voltage divided by the characteristic resistance of the material. The magnetic field of this eddy current must be significantly smaller than the fields being measured. For an aluminum sample with $A = 9 \times 10^{-6}\,\mathrm{m}^2$, $t = 0.1\,\mathrm{mm}$ and the frequency of the scanned field at 20 Hz, we estimate the secondary magnetic field generated in the sample to be a few nanotesla. This secondary magnetic field is small compared to the field measured in the conductive cross pattern, which is on the order of a few millitesla.

The measured sensitivity with the zero-field technique is comparable to that obtained with the cw ODMR and GSLAC techniques. We stress that the zero-field microwave-free technique is not optimal since the technique used here is analogous to cw ODMR, which is not the most sensitive dc magnetometer. In addition, our objective is to improve the sensitivity of our magnetometer by optimizing the experimental setup. However, how to improve its sensitivity with the material engineering of nanodiamonds remains unclear.

ACKNOWLEDGMENTS

This work was supported by the European Commission's Horizon Europe Framework Program under the Research and Innovation Action MUQUABIS GA No.

101070546, by the German Federal Ministry of Education and Research (BMBF) within the Quantumtechnologien program (DIAQNOS, Project No. 13N16455) and by the German DFG, Project SFB 1552 "Defekte und Defektkontrolle in weicher Materie." The study was carried out using research infrastructure purchased with the funds of the European Union in the framework of the Smart Growth Operational Programme, Measure 4.2; Grant No. POIR.04.02.00-00-D001/20, "ATOMIN 2.0 – ATOMic scale science for the INnovative economy". This research was funded in part by the National Science Centre, Poland, Grant No. 2020/39/I/ST3/02322 and Grant No. 2023/05/Y/ST3/00135 within the QuantERA II Programme that has received funding from the European Union's Horizon 2020 research and innovation programme under Grant Agreement No. 101017733. For the purpose of Open Access, the author has applied a CC-BY public copyright licence to any Author Accepted Manuscript (AAM) version arising from this submission.

DATA AVAILABILITY

The supporting data for this article are openly available in the Zenodo data repository [43].

[1] Á. Gali, Ab initio theory of the nitrogen-vacancy center in diamond, Nanophotonics **8**, 1907 (2019).

[2] K.-M. C. Fu, G. Z. Iwata, A. Wickenbrock, and D. Budker, Sensitive magnetometry in challenging environments, AVS Quantum Sci. **2**, 044702 (2020).

[3] J. Wang, F. Feng, J. Zhang, J. Chen, Z. Zheng, L. Guo, W. Zhang, X. Song, G. Guo, L. Fan, *et al.*, High-sensitivity temperature sensing using an implanted single nitrogen-vacancy center array in diamond, Phys. Rev. B **91**, 155404 (2015).

[4] K. O. Ho, K. C. Wong, M. Y. Leung, Y. Y. Pang, W. K. Leung, K. Y. Yip, W. Zhang, J. Xie, S. K. Goh, and S. Yang, Recent developments of quantum sensing under pressurized environment using the nitrogen vacancy (NV) center in diamond, J. Appl. Phys. **129**, 241101 (2021).

[5] A. Kuwahata, T. Kitaizumi, K. Saichi, T. Sato, R. Igarashi, T. Ohshima, Y. Masuyama, T. Iwasaki, M. Hatano, F. Jelezko, *et al.*, Magnetometer with nitrogen-vacancy center in a bulk diamond for detecting magnetic nanoparticles in biomedical applications, Sci. Rep. **10**, 2483 (2020).

[6] F. Dolde, H. Fedder, M. W. Doherty, T. Nöbauer, F. Rempp, G. Balasubramanian, T. Wolf, F. Reinhard, L. C. Hollenberg, F. Jelezko, *et al.*, Electric-field sensing using single diamond spins, Nat. Phys. **7**, 459 (2011).

[7] J. F. Barry, M. H. Steinecker, S. T. Alsid, J. Majumder, L. M. Pham, M. F. O'Keeffe, and D. A. Braje, Sensitive ac and dc magnetometry with nitrogen-vacancy-center ensembles in diamond, Phys. Rev. Appl. **22**, 044069 (2024).

[8] J. F. Barry, M. J. Turner, J. M. Schloss, D. R. Glenn, Y. Song, M. D. Lukin, H. Park, and R. L. Walsworth, Optical magnetic detection of single-neuron action potentials using quantum defects in diamond, Proc. Natl. Acad. Sci. **113**, 14133 (2016).

[9] T. Lenz, G. Chatzidrosos, Z. Wang, L. Bougas, Y. Dumeige, A. Wickenbrock, N. Kerber, J. Zázvorka, F. Kammerbauer, M. Kläui, Z. Kazi, K.-M. C. Fu, K. M. Itoh, H. Watanabe, and D. Budker, Imaging topological spin structures using light-polarization and magnetic microscopy, Phys. Rev. Appl. **15**, 024040 (2021).

[10] A. Nowodzinski, M. Chipaux, L. Toraille, V. Jacques, J.-F. Roch, and T. Debuisschert, Nitrogen-vacancy centers in diamond for current imaging at the redistributive layer level of integrated circuits, Microelectron. Reliab. **55**, 1549 (2015).

[11] E. V. Levine, M. J. Turner, P. Kehayias, C. A. Hart, N. Langellier, R. Trubko, D. R. Glenn, R. R. Fu, and R. L. Walsworth, Principles and techniques of the quantum diamond microscope, Nanophotonics **8**, 1945 (2019).

[12] J. W. Blanchard, D. Budker, and A. Trabesinger, Lower than low: Perspectives on zero- to ultralow-field nuclear magnetic resonance, J. Magn. Reson. **323**, 106886 (2021).

[13] D. A. Simpson, J.-P. Tetienne, J. M. McCoey, K. Ganesan, L. T. Hall, S. Petrou, R. E. Scholten, and L. C. Hollenberg, Magneto-optical imaging of thin magnetic films using spins in diamond, Sci. Rep. **6**, 1 (2016).

[14] H. Clevenson, E. H. Chen, F. Dolde, C. Teale, D. Englund, and D. Braje, Diamond-nitrogen-vacancy electronic and nuclear spin-state anticrossings under weak transverse magnetic fields, Phys. Rev. A **94**, 021401(R) (2016).

[15] S. V. Anishchik, V. G. Vins, A. P. Yelisseyev, N. N. Lukzen, N. L. Lavrik, and V. A. Bagryansky, Low-field feature in the magnetic spectra of NV-centers in diamond, New J. Phys. **17**, 023040 (2015).

[16] R. Akhmedzhanov, L. Gushchin, N. Nizov, V. Nizov, D. Sobgayda, I. Zelensky, and P. Hemmer, Microwave-free magnetometry based on cross-relaxation resonances in diamond nitrogen-vacancy centers, Phys. Rev. A **96**, 013806 (2017).

[17] S. Saijo, Y. Matsuzaki, S. Saito, T. Yamaguchi, I. Hanano, H. Watanabe, N. Mizuochi, and J. Ishi-Hayase, Ac magnetic field sensing using continuous-wave optically detected magnetic resonance of nitrogen-vacancy centers in diamond, Appl. Phys. Lett. **113**, 082405 (2018).

[18] A. Wickenbrock, H. Zheng, L. Bougas, N. Leefer, S. Afach, A. Jarmola, V. M. Acosta, and D. Budker, Microwave-free magnetometry with nitrogen-vacancy centers in diamond, Appl. Phys. Lett. **109**, 053505 (2016).

[19] R. Staacke, R. John, R. Wunderlich, L. Horsthemke, W. Knolle, C. Laube, P. Glösekötter, B. Burchard, B. Abel, and J. Meijer, Isotropic scalar quantum sensing of magnetic fields for industrial application, Adv. Quantum Technol. **3**, 2000037 (2020).

[20] R. Wunderlich, R. Staacke, W. Knolle, B. Abel, and J. Meijer, Magnetic field and angle-dependent photoluminescence of a fiber-coupled nitrogen vacancy rich diamond, J. Appl. Phys. **130**, 124901 (2021).

[21] H. Zheng, Z. Sun, G. Chatzidrosos, C. Zhang, K. Nakamura, H. Sumiya, T. Ohshima, J. Isoya, J. Wrachtrup, A. Wickenbrock, and D. Budker, Microwave-free vector magnetometry with nitrogen-vacancy centers along a single axis in diamond, Phys. Rev. Appl. **13**, 044023 (2020).

[22] J. Shaji Rebeirro, M. Omar, T. Lenz, O. Dhungel, P. Blümler, D. Budker, and A. Wickenbrock, Microwave-free

wide-field magnetometry using nitrogen-vacancy centers, Phys. Rev. Appl. **21**, 044039 (2024).

[23] L. Rondin, J.-P. Tetienne, T. Hingant, J.-F. Roch, P. Maletinsky, and V. Jacques, Magnetometry with nitrogen-vacancy defects in diamond, Rep. Prog. Phys. **77**, 056503 (2014).

[24] M. Mrózek, D. Rudnicki, P. Kehayias, A. Jarmola, D. Budker, and W. Gawlik, Longitudinal spin relaxation in nitrogen-vacancy ensembles in diamond, EPJ Quantum Technol. **2**, 1 (2015).

[25] J. W. Blanchard and D. Budker, Zero-to ultralow-field NMR, Emagres **5**, 1395 (2007).

[26] E. van Oort and M. Glasbeek, Cross-relaxation dynamics of optically excited N-V centers in diamond, Phys. Rev. B **40**, 6509 (1989).

[27] M. C. Cambria, A. Norambuena, H. T. Dinani, G. Thiering, A. Gardill, I. Kemeny, Y. Li, V. Lordi, A. Gali, J. R. Maze, and S. Kolkowitz, Temperature-dependent spin-lattice relaxation of the nitrogen-vacancy spin triplet in diamond, Phys. Rev. Lett. **130**, 256903 (2023).

[28] J. Choi, S. Choi, G. Kucsko, P. C. Maurer, B. J. Shields, H. Sumiya, S. Onoda, J. Isoya, E. Demler, F. Jelezko, N. Y. Yao, and M. D. Lukin, Depolarization dynamics in a strongly interacting solid-state spin ensemble, Phys. Rev. Lett. **118**, 093601 (2017).

[29] C. Pellet-Mary, M. Perdriat, P. Huillery, and G. Hétet, Relaxation processes in dipole-coupled nitrogen-vacancy centers in zero field: Application in magnetometry, Phys. Rev. Appl. **20**, 034050 (2023).

[30] O. Dhungel, T. Lenz, M. Omar, J. S. Rebeirro, M.-T. Luu, A. T. Younesi, R. Ulbricht, V. Ivády, A. Gali, A. Wickenbrock, and D. Budker, Near zero-field microwave-free magnetometry with ensembles of nitrogen-vacancy centers in diamond, Phys. Rev. B **109**, 224107 (2024).

[31] O. Dhungel, M. Mrózek, T. Lenz, V. Ivády, A. Gali, A. Wickenbrock, D. Budker, W. Gawlik, and A. M. Wojciechowski, Near-zero-field microwave-free magnetometry with nitrogen-vacancy centers in nanodiamonds, Opt. Express **32**, 21936 (2024).

[32] W. S. Huxter, M. L. Palm, M. L. Davis, P. Welter, C.-H. Lambert, M. Trassin, and C. L. Degen, Scanning gradiometry with a single spin quantum magnetometer, Nat. Commun. **13**, 3761 (2022).

[33] A. Filipkowski, M. Mrózek, G. Stępniewski, J. Kierdaszuk, A. Drabińska, T. Karpate, M. Głowacki, M. Ficek, W. Gawlik, R. Buczyński, *et al.*, Volumetric incorporation of NV diamond emitters in nanostructured F2 glass magneto-optical fiber probes, Carbon **196**, 10 (2022).

[34] Z. Mi, C.-B. Chen, H. Q. Tan, Y. Dou, C. Yang, S. P. Turaga, M. Ren, S. K. Vajandar, G. H. Yuen, T. Osipowicz, *et al.*, Quantifying nanodiamonds biodistribution in whole cells with correlative iono-nanoscopy, Nat. Commun. **12**, 4657 (2021).

[35] Y. Chen, Q. Lin, H. Cheng, H. Huang, J. Shao, Y. Ye, G.-S. Liu, L. Chen, Y. Luo, and Z. Chen, Nanodiamond-based optical-fiber quantum probe for magnetic field and biological sensing, ACS Sens. **7**, 3660 (2022).

[36] S. Sengottuvel, M. Mrózek, M. Sawczak, M. J. Głowacki, M. Ficek, W. Gawlik, and A. M. Wojciechowski, Wide-field magnetometry using nitrogen-vacancy color centers with randomly oriented micro-diamonds, Sci. Rep. **12**, 17997 (2022).

[37] S. J. DeVience, L. M. Pham, I. Lovchinsky, A. O. Sushkov, N. Bar-Gill, C. Belthangady, F. Casola, M. Corbett, H. Zhang, M. Lukin, *et al.*, Nanoscale NMR spectroscopy and imaging of multiple nuclear species, Nat. Nanotechnol. **10**, 129 (2015).

[38] M. Barbiero, S. Castelletto, Q. Zhang, Y. Chen, M. Charnley, S. Russell, and M. Gu, Nanoscale magnetic imaging enabled by nitrogen vacancy centres in nanodiamonds labelled by iron–oxide nanoparticles, Nanoscale **12**, 8847 (2020).

[39] G. Kucsko, P. C. Maurer, N. Y. Yao, M. Kubo, H. J. Noh, P. K. Lo, H. Park, and M. D. Lukin, Nanometre-scale thermometry in a living cell, Nature **500**, 54 (2013).

[40] M. Ortner and L. G. C. Bandeira, Magpylib: A free python package for magnetic field computation, SoftwareX **11**, 100466 (2020).

[41] J. F. Barry, J. M. Schloss, E. Bauch, M. J. Turner, C. A. Hart, L. M. Pham, and R. L. Walsworth, Sensitivity optimization for NV-diamond magnetometry, Rev. Mod. Phys. **92**, 015004 (2020).

[42] A. Dréau, M. Lesik, L. Rondin, P. Spinicelli, O. Arcizet, J.-F. Roch, and V. Jacques, Avoiding power broadening in optically detected magnetic resonance of single NV defects for enhanced dc magnetic field sensitivity, Phys. Rev. B **84**, 195204 (2011).

[43] S. Sengottuvel, O. Dhungel, M. Mrózek, and A. M. Wojciechowski, Dataset for the article "Microwave-free imaging magnetometry with nitrogen-vacancy centers in nanodiamonds at near-zero field", Zenodo, https://doi.org/10.5281/zenodo.14833488 (2025).